In vivo photoacoustic chorioretinal vascular imaging in albino mouse

Wei Song (宋 伟)[1,2*], Qing Wei (魏 青)[2], Rui Zhang (张 锐)[1], and Hao F. Zhang (张 浩)[2]**

[1] *Condensed Matter Science and Technology Institute, Harbin Institute of Technology, Harbin 150080, China*

[2] *Department of Biomedical Engineering, Northwestern University, Evanston, IL 60208, USA*

[*] *Corresponding author: weisong1220@gmail.com;*

[**] *corresponding author: hfzhang@northwestern.edu*

Received January 24, 2014; accepted March 27, 2014; posted online April 30, 2014

Photoacoustic ophthalmoscopy (PAOM) is a novel imaging modality, which is capable of non-invasively detecting optical absorption properties in the retina. We visualize the microvasculature in retina and choroid in albino mouse using PAOM guided by spectral-domain optical coherence tomography. Since albino mouse characterizes by lacking melanin in retinal pigment epithelium (RPE), PAOM illumination laser can penetrate through the RPE onto choroid, and consequently provides volumetric visualization of chorioretinal vasculatures as a result of strong hemoglobin optical absorption. The high-quality chorioretinal microvascular imaging acquired by PAOM implies its great potential in understanding pathological mechanisms and developing therapeutic strategies for major chorioretinal diseases that correlate with vascular disorders.

OCIS codes: 170.5120, 170.4470, 170.0110, 170.4500.

doi: 10.3788/COL201412.051704.

Mouse models are critical laboratory animal models for investigating many ocular disorders because it has well-characterized genomes with many genetically defined strains and well-developed genetic manipulation approaches, which are not yet available in other mammals[1,2]. The development of mouse models with various visual system abnormalities greatly benefits the understanding and treatment of major ocular diseases[3−5]. Although retinal morphology can be characterized quantitatively by histologic examination in terminal experiments, non-invasive imaging method is preferred because it permits longitudinal evaluation of disease progression in individual animal subjects. Existing imaging modalities, including fundus photography, fluorescence/autofluorescence imaging, confocal scanning-laser ophthalmoscopy (cSLO), and optical coherence tomography (OCT), contribute significantly in monitoring retinal disease onset and progression, as well as therapeutic response[6−8]. However, they are predominantly dependent on the back-reflected photons or emitted fluorescent light from the retina; therefore, the retinal pathophysiology information, which is specifically associated with tissue optical absorption properties, might be inaccessible by these traditional imaging technologies.

Photoacoustic (PA) imaging is capable of mapping optical energy deposition in biological tissue through detecting the thermo-elastically induced acoustic waves as a result of strong optical absorption by endogenous biomolecules or exogenous contrast agents[9−12]. Recently, photoacoustic microscopy (PAM) is introduced in ophthalmologic imaging for rodent eyes, which offers optical-absorption-based anatomic and functional information that is complementary to the conventional imaging modalities[13−17]. As an extension of optical-resolution PAM, newly-developed photoacoustic ophthalmoscopy (PAOM) takes advantage of laser-scanning pattern and unfocused ultrasonic detection, and thus enables the *in vivo* structural imaging for the posterior segment of rodent eyes, including retinal/choroidal vessels (RV/CV) and melanin in retinal pigmented epithelium (RPE)[14−17]. PAOM has multiple advantages including label free, high scanning speed, volumetric capability, and physiologically-specific optical-absorption contrast. Moreover, PAOM is readily compatible with the well-established clinical ophthalmological imaging techniques (i.e., OCT, and SLO, etc.) for providing comprehensive evaluation of physiological and pathological status in the retina[15−17].

Among mouse models, albino mouse eye is increasingly utilized to investigate the pathological mechanisms of human blinding diseases due to its lack of pigmentation[3−5]. In this work, we report on *in vivo* imaging of albino mouse eyes through an integrated PAOM and spectrum-domain OCT (SD-OCT) system. Guided by SD-OCT, PAOM acquires volumetric visualization of the retina and choroid microvascular networks.

Figure 1 shows the schematic diagram of the *in vivo* multimodal mouse retinal imaging system, which is described in detail previously[17]. In brief, a 532-nm frequency-doubled Nd:YAG laser (SPOT-10-100, Elforlight Ltd, UK) with 2-ns pulse duration was used as the PAOM excitation source, and a broadband superluminescent diode (SLD, IPSDD0804, InPhenix, USA; 840-nm center wavelength; 50-nm bandwidth) was employed as the SD-OCT source. The PAOM illumination laser and the SD-OCT probing light were combined by a hot mirror (HM, FM02, Thorlabs, USA), which were then scanned by a galvanometer (GM, QS-7, Nutfield Technology, USA) and delivered into the eye posterior with a telescope configuration (L1 and L2). The laser-induced PA waves from the animal retina were detected by an unfocused needle ultrasonic transducer

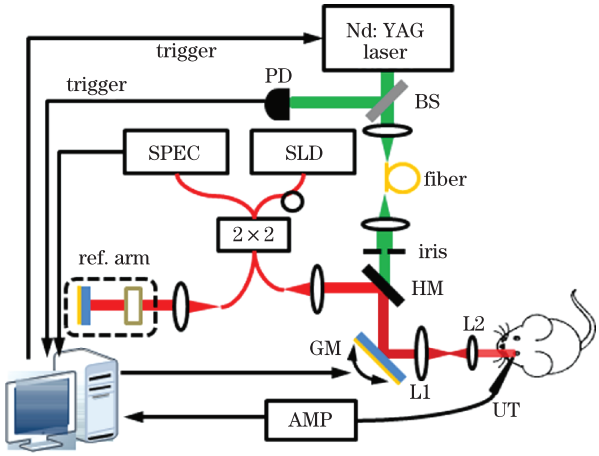

Fig. 1. (Color online) Schematic diagram of the *in vivo* ophthalmic imaging system that integrates PAOM and SD-OCT. ref. arm: OCT reference arm; 2×2: 50:50 fiber coupler; SPEC: spectrometer; BS: beam splitter; AMP: amplifier; UT: ultrasonic transducer.

(40-MHz central frequency, 16-MHz bandwidth), which was gently placed in contact with the animal eyelid through ultrasound coupling gel. The amplified PA signals were digitized by a data acquisition board (200-MS/s sampling rate, CS14200, Gage Applied, Canada) triggered by signal of a photodiode (PD, DET10A, Thorlabs, USA). In the SD-OCT sub-system, the reflected photons from the reference arm and mouse retina were recorded using a home-built spectrometer. In the PAOM sub-system, we introduced an iris to adjust the laser beam diameter onto the animal pupil plane for a proper effective numerical aperture.

PAOM excitation laser energy was ~40 nJ per pulse, and SD-OCT probing light power was 0.8 mW, both of which were shown to be within the American National Standards Institude (ANSI) laser safety limit[14]. An analogue output board (PCI-6731, National Instruments, USA) was used to synchronize the PAOM and OCT sub-system. Also, it triggered both the PAOM laser firing and OCT signal acquisition, and controlled the galvanometer scanning. The present system has an A-line rate of 24 kHz, which takes only 2.7 s for simultaneously acquiring the PAOM and SD-OCT images (consisting of 256 B-scans with 256 A-lines per B-scan).

We performed *in vivo* retinal imaging in Swiss Webster albino mice (Harlan Laboratories, USA). The mice were anesthetized by intraperitoneal injection of a mixture of ketamine (87 mg/kg body weight) and xylazine (13 mg/kg body weight). Afterwards, we applied 0.5% tetracaine hydrochloride ophthalmic solution to paralyze the iris sphincter muscle, and 1% tropicamide ophthalmic solution to dilate the pupil. During imaging, commercial artificial tears were applied to the animal's eye every other minute to prevent the cornea dehydration and cataract formation.

All experiments were performed in compliance with the Association for Research in Vision and Ophthalmology (ARVO) Statement for the Use of Animals in Ophthalmic and Vision Research, as well as the laboratory animal protocol approved by the Animal Care and Use Committee of Northwestern University. For eye safety concern, we set the whole imaging duration less than 5 min, including OCT alignment, the transducer orientation adjustment, and data acquisition. Follow-up examinations using OCT showed no noticeable retinal damages in imaged animals.

In this work, we initially identified the region of interest through the guidance of the real-time SD-OCT B-scan display while blocking the PAOM illumination. Afterwards, both imaging modalities were activated simultaneously to acquire three-dimensional (3D) dataset. Figure 2 shows the fundus images of SD-OCT and PAOM from an albino mouse eye. In order to exhibit the choroidal vasculatures clearly, we intentionally placed the optic disc off-center within the field of view where the RV density is low. In addition, the PAOM laser focus was carefully adjusted beneath the RV for imaging both retinal and choroidal vasculatures.

In the OCT *en face* image (Fig. 2(a)), the RV appear dark because few probing photons can be back-scattered due to the optical absorption of hemoglobin. In addition, they display a blurred appearance, which may be associated with the deteriorated optical focus caused by the severe mouse eye aberration[18]. In comparison, PAOM demonstrates a better contrast for imaging the RV and CV (in Fig. 2(b)) due to the dominating absorber of hemoglobin at the 532-nm illumination wavelength. In albino eyes, the concentration of melanin is minimal in RPE. As a result, PAOM excitation light can penetrate through the RPE layer, and generate high-amplitude PA signals from CV. This is different from the images from normal mouse eyes[17], where PAOM cannot visualize choroid due to high-concentration RPE melanin absorbing the excitation laser. The fundus images from both PAOM and OCT modalities registered naturally because they have same laser scanning and delivery mechanisms, and the synchronized data acquisition.

Figures 2(c) and (d) illustrate the simultaneously acquired B-scan images of SD-OCT and PAOM, respectively. The dashed-line in Fig. 2(a) indicates their corresponding retinal location. In PAOM B-scan image (Fig. 2(d)), we observe the upper RV, which primarily perfuse the inner retina, and the CV locating behind the retina, which is responsible for supplying the RPE cells and photoreceptors[19]. Abnormalities in the retinal and choroidal circulations may result in several blinding diseases, such as diabetic retinopathy and macular degeneration[19,20]. Unlike PAOM, OCT cross-section retinal image (Fig. 2(c)) offers much more anatomic information, including the retinal nerve fiber layer (RFNL), the photoreceptor inner and outer segment junction (IS/OS), and the complex of RPE and choroid (RPE+C), because the individual layer has different optical scattering coefficients and refractive indexes. The difference between the two imaging modalities mainly comes from their different imaging contrast mechanisms. Since the optical absorption coefficients of these multiple retinal layers are very low[21], their PA signals are undetectable in PAOM. On the other hand, PAOM has much worse axial resolution than OCT (23 and 6 μm, respectively), and thus it cannot resolve the fine layers.

Figure 3 demonstrates the volumetric imaging capability of PAOM. To show the RV and CV independently, the PAOM 3D raw dataset is manually segmented taking

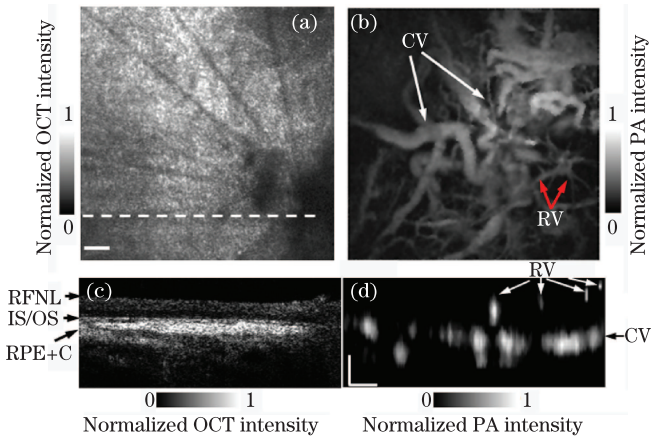

Fig. 2. (Color online) *In vivo* simultaneous SD-OCT and PAOM imaging of an albino mouse eye. Fundus images acquired by (a) SD-OCT and (b) PAOM, respectively; B-scan images acquired by (c) SD-OCT and (d) PAOM, at the location highlighted by the dashed line in Fig. 2(a). Bar: 100 μm.

advantage of PA waves from multiple optical-absorption layers with different time-of-flight. The RV pseudo-colored in red present a star-shaped architecture, which is much more visible than that in the original PAOM fundus image (Fig. 2(b)). The diameter of these RV estimated at about 30 μm or less (nearly equal with PAOM transverse resolution of ~20 μm), suggesting that some vessels only occupy one single pixel in PAOM image. As a result, their PA signals may drop into noise level of the needle ultrasound detector. To obtain a better visualization of the RV, novel detector with much lower noise equivalent pressure values, such as the optical micro-ring resonator[22], is desired. Besides, adaptive optics can be adopted to improve the PAOM lateral resolution by correcting the animal ocular aberrations[18]. In Fig. 3(b), PAOM visualizes dense choroid vascular bed (pseudo-colored in green), which has more complicated structure compared to the sparse RV. Other than the major CV (pointed out by arrow groups 1), some tiny choriocapillaris can be observed as indicated by arrow groups 2. Figure 3(c) shows a clearer chorioretinal vascular anatomy by overlying the segmented RV onto CV. This observation from PAOM corresponds well with the reported retina-choroid circulation anatomy in the rodent eyes. Further, we provide a movie (media 1) displaying the chorioretinal vasculatures from different viewing angles in Fig. 3(d).

Previously, we demonstrated the capability of PAOM for *in vivo* imaging chorioretinal micro-vascular networks in albino rats[15,16]. Compared with rats, it is more challenging to obtain mouse retinal anatomy because of its very small pupils and rapid cataract formation[8]. The laser delivery alignment becomes harder owing to the much smaller pupil size of mouse eye, which also degrades the signal-to-noise ratio due to less back-reflected photons from the retina. The cataract in mouse eye leads to lower laser transmission efficiency, and consequently the retinal imaging quality may be deteriorated[7]. In addition, mouse has stronger eye aberration[18], making the retinal imaging more difficult than in rat. However, the extension of PAOM for acquiring the retinal anatomy in mouse models is desired because the genetic manipulation approaches in mice are more readily available compared to rats[1,2].

Note that the current PAOM is limited to imaging choroid vasculatures in albino eyes, where low-concentration melanin in RPE permits PAOM illuminating laser to penetrate deeper into the choroid. In pigmented animals, however, the RPE has very dense melanin, which strongly absorbs the visible PAOM illuminating laser. As a result, it is insufficient to reconstruct the CV image. On the other hand, high-amplitude PA waves are produced due to high optical absorption coefficient of RPE melanin. In our early work (Figs. 2(b) and 2(e) in Ref. [17]), PAOM provides a clear visualization of RPE melanin in addition to the RV in normal mouse eyes, while no signal is detected from CV. A potential solution is to administer indocyanine green (ICG) as contrast agent and to simultaneously tune PAOM excitation light to near-infrared (NIR) spectral range. Because ICG characterizes by moderate fluorescent quantum yield (~10%) and excitation wavelength at NIR spectrum range, the high-amplitude PA signals can be produced from deeper vasculatures perfused by ICG solution[23]. In the future, we aim to develop ICG-based PAOM for imaging the choroidal vasculatures that are behind the melanin-packed RPE in pigmented eyes.

In conclusion, we demonstrate the capability of *in vivo* imaging chorioretinal vasculature in albino mouse eyes using PAOM guided by SD-OCT. Although both strong eye aberration and much smaller vessels make the retinal imaging difficult, PAOM provides well-resolved microvascular anatomy based on its optical-absorption imaging mechanism.

This work was supported in part by the National "973" Program of China (No. 2013CB632900), the National

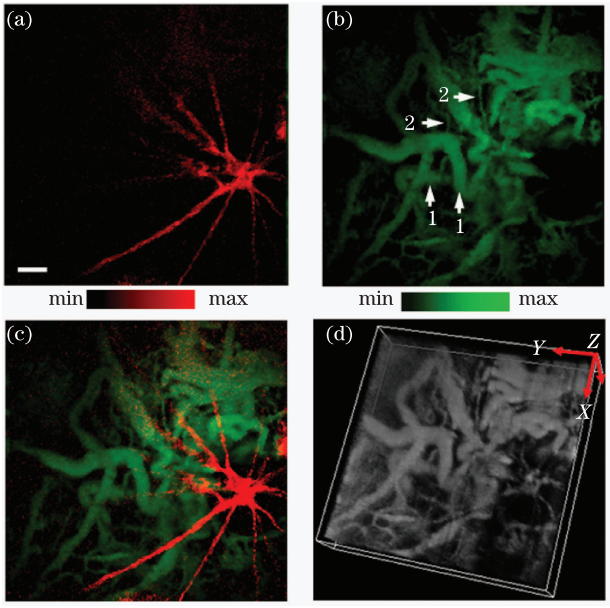

Fig. 3. (Color online) Volumetric imaging of RV and CV by PAOM. Segmented PAOM images of (a) RV (pseudo-colored in red) and (b) CV (pseudo-colored in green). Arrow groups 1 and 2 in the panel b indicate a few major CV and choriocapillaris, respectively. (c) Overlaid PAOM chorioretinal vascular image. (d) 3D visualization of PAOM chorioretinal vascular anatomy (media 1). Bar: 100 μm.

Natural Science Foundation of China (No. 50602009), the U.S. NIH grants RC4EY021357 and R01EY019951, andU.S. NSF grant CBET-1055379 and CBET-1066776.

References

1. A. Stahl, K. M. Connor, P. Sapieha, J. Chen, R. J. Dennison, N. M. Krah, M. R. Seaward, K.L. Willett, C. M. Aderman, K. I. Guerin, J. Hua, C. Löqvist, A. Hellström, and L. E. H. Smith, Invest. Ophthalmol. Vis. Sci. **51,** 2813 (2010).
2. B. Chang, N. Hawes, R. Hurd, J. Wang, D. Howell, M. Davisson, T. Roderick, S. Nusinowitz, and J. Heckenlively, Vis. Neurosci. **22,** 587 (2005).
3. G. Traber, C Chen, Y. Huang, M. Spoor, J. Roos, M. Frens, D. Straumann, and C. Grimm, Invest. Ophthalmol. Vis. Sci. **53,** 5737 (2012).
4. C. Zhao, D. Yasumura, X. Li, M. Matthes, M. Lloyd, G. Nielsen, K. Ahern, M. Snyder, D. Bok, J. Dunaief, M. LaVail, and D.Vollrath, J. Clin. Invest. **121,** 369 (2011).
5. A. B. Condren, A. Kumar, P. Mettu, K. J. Liang, L. Zhao, J. Tsai, R. N. Fariss, and W. T. Wong, PLoS One **8,** e53386 (2013).
6. M. Koronyo-Hamaoui, Y. Koronyo, A. Ljubimov, C. Miller, M.Ko, K. Black, M. Schwartz, and D. Farkas, Neuroimage. **54,** S204 (2011).
7. M. Paques, M. Simonutti. M. Roux, S. Picaud, E. Levavasseur, C. Bellman, and J. Sahel, Vision. Res. **46,** 1336 (2006).
8. M. Ruggeri, H. Wehbe, S. Jiao, G. Gregori, M. Jockovich, A. Hackam, Y. Duan, and C. Puliafito, Invest. Ophthalmol. Vis. Sci. **48,** 1808 (2007).
9. L. Wang, Nat. Photon. **3,** 503 (2009).
10. L. Wang andS. Hu, Science **335,** 1458 (2012).
11. Y. Gao, Y. Deng, X. Tong, H. Wang, Z. Deng, X. Yang, Y. Liu, H. Gong, and Q. Luo, Chin. Opt. Lett. **10,** 061101 (2012).
12. S. Ye, J. Yang, J. Xi, Q. Ren, and C. Li, Chin. Opt. Lett. **10,** 121701 (2012).
13. S. Hu, B. Rao, K. Maslov, and L. Wang, Opt Lett. **35,** 1 (2010).
14. S. Jiao, M. Jiang, J. Hu, A. Fawzi, Q. Zhou, K. Shung, C. Puliafito, and H. Zhang, Opt. Express **18,** 3967 (2010).
15. W. Song, Q. Wei, T. Liu, D. Kuai, J. Burke, S. Jiao, and H. Zhang, J. Biomed. Opt. **17,** 061206 (2012).
16. T. Liu, Q. Wei, W. Song, J. M. Burke, S. Jiao, and H. F. Zhang, Biomed. Opt. Express. **3,** 792 (2012).
17. W. Song, Q. Wei, L. Feng, V. Sarthy, S. Jiao, X. Liu, and H. F. Zhang, J. Biophoton. **6,** 505 (2013).
18. Y. Geng, L.Schery, R. Sharma, A. Dubra, K. Ahmad, R. Libby, and D. Williams, Biomed. Opt. Express **2,** 717 (2011).
19. D. Yu and S. Cringle, Prog. Retin. Eye. Res. **20,** 175 (2001).
20. M. Zarbin, Arch. Ophthalmol. **122,** 598 (2004).
21. M. Hammer, A. Roggan, D. Schweitzer, and G. Muller, Phys. Med. Biol. **40,** 963 (1995).
22. H. Li, B. Dong, Z. Zhang, H. F. Zhang, and C. Sun, "A transparent broadband ultrasonic detector based on optical micro-ring resonator for functional photoacoustic imaging," Scientific Reports, to be published (2014).
23. C. Kim, K. H. Song, F. Gao, and L. V. Wang, Radiology **255,** 442 (2010).